

**Centrality dependence of charged hadron production
in deuteron+gold and nucleon+gold collisions at $\sqrt{s_{NN}} = 200$ GeV**

S.S. Adler,⁵ S. Afanasiev,²⁰ C. Aidala,¹⁰ N.N. Ajitanand,⁴⁴ Y. Akiba,^{21,40} A. Al-Jamel,³⁵ J. Alexander,⁴⁴ K. Aoki,²⁵ L. Aphecetche,⁴⁶ R. Armendariz,³⁵ S.H. Aronson,⁵ R. Averbeck,⁴⁵ T.C. Awes,³⁶ V. Babintsev,¹⁷ A. Baldisseri,¹¹ K.N. Barish,⁶ P.D. Barnes,²⁸ B. Bassalleck,³⁴ S. Bathe,^{6,31} S. Batsouli,¹⁰ V. Baublis,³⁹ F. Bauer,⁶ A. Bazilevsky,^{5,41} S. Belikov,^{19,17,*} M.T. Bjorndal,¹⁰ J.G. Boissevain,²⁸ H. Borel,¹¹ M.L. Brooks,²⁸ D.S. Brown,³⁵ N. Bruner,³⁴ D. Bucher,³¹ H. Buesching,^{5,31} V. Bumazhnov,¹⁷ G. Bunce,^{5,41} J.M. Burward-Hoy,^{28,27} S. Butsyk,⁴⁵ X. Camard,⁴⁶ P. Chand,⁴ W.C. Chang,² S. Chernichenko,¹⁷ C.Y. Chi,¹⁰ J. Chiba,²¹ M. Chiu,¹⁰ I.J. Choi,⁵³ R.K. Choudhury,⁴ T. Chujo,⁵ V. Cianciolo,³⁶ Z. Citron,⁴⁵ Y. Cobigo,¹¹ B.A. Cole,¹⁰ M.P. Comets,³⁷ P. Constantin,¹⁹ M. Csanád,¹³ T. Csörgő,²² J.P. Cussonneau,⁴⁶ D. d'Enterria,¹⁰ K. Das,¹⁴ G. David,⁵ F. Deák,¹³ H. Delagrange,⁴⁶ A. Denisov,¹⁷ A. Deshpande,⁴¹ E.J. Desmond,⁵ A. Devismes,⁴⁵ O. Dietzsch,⁴² J.L. Drachenberg,¹ O. Drapier,²⁶ A. Drees,⁴⁵ A. Durum,¹⁷ D. Dutta,⁴ V. Dzhordzhadze,⁴⁷ Y.V. Efremenko,³⁶ H. En'yo,^{40,41} B. Espagnon,³⁷ S. Esumi,⁴⁹ D.E. Fields,^{34,41} C. Finck,⁴⁶ F. Fleuret,²⁶ S.L. Fokin,²⁴ B.D. Fox,⁴¹ Z. Fraenkel,⁵² J.E. Frantz,¹⁰ A. Franz,⁵ A.D. Frawley,¹⁴ Y. Fukao,^{25,40,41} S.-Y. Fung,⁶ S. Gadrat,²⁹ M. Germain,⁴⁶ A. Glenn,⁴⁷ M. Gonin,²⁶ J. Gosset,¹¹ Y. Goto,^{40,41} R. Granier de Cassagnac,²⁶ N. Grau,¹⁹ S.V. Greene,⁵⁰ M. Grosse Perdekamp,^{18,41} H.-Å. Gustafsson,³⁰ T. Hachiya,¹⁶ J.S. Haggerty,⁵ H. Hamagaki,⁸ A.G. Hansen,²⁸ E.P. Hartouni,²⁷ M. Harvey,⁵ K. Hasuko,⁴⁰ R. Hayano,⁸ X. He,¹⁵ M. Heffner,²⁷ T.K. Hemmick,⁴⁵ J.M. Heuser,⁴⁰ P. Hidas,²² H. Hiejima,¹⁸ J.C. Hill,¹⁹ R. Hobbs,³⁴ W. Holzmann,⁴⁴ K. Homma,¹⁶ B. Hong,²³ A. Hoover,³⁵ T. Horaguchi,^{40,41,48} T. Ichihara,^{40,41} V.V. Ikonnikov,²⁴ K. Imai,^{25,40} M. Inaba,⁴⁹ M. Inuzuka,⁸ D. Isenhower,¹ L. Isenhower,¹ M. Ishihara,⁴⁰ M. Issah,⁴⁴ A. Isupov,²⁰ B.V. Jacak,^{45,†} J. Jia,⁴⁵ O. Jinnouchi,^{40,41} B.M. Johnson,⁵ S.C. Johnson,²⁷ K.S. Joo,³² D. Jouan,³⁷ F. Kajihara,⁸ S. Kametani,^{8,51} N. Kamihara,^{40,48} M. Kaneta,⁴¹ J.H. Kang,⁵³ K. Katou,⁵¹ T. Kawabata,⁸ A.V. Kazantsev,²⁴ S. Kelly,^{9,10} B. Khachaturov,⁵² A. Khanzadeev,³⁹ J. Kikuchi,⁵¹ D.J. Kim,⁵³ E. Kim,⁴³ G.-B. Kim,²⁶ H.J. Kim,⁵³ E. Kinney,⁹ A. Kiss,¹³ E. Kistenev,⁵ A. Kiyomichi,⁴⁰ C. Klein-Boesing,³¹ H. Kobayashi,⁴¹ L. Kochenda,³⁹ V. Kochetkov,¹⁷ R. Kohara,¹⁶ B. Komkov,³⁹ M. Konno,⁴⁹ D. Kotchetkov,⁶ A. Kozlov,⁵² P.J. Kroon,⁵ C.H. Kuberg,^{1,*} G.J. Kunde,²⁸ K. Kurita,⁴⁰ M.J. Kweon,²³ Y. Kwon,⁵³ G.S. Kyle,³⁵ R. Lacey,⁴⁴ J.G. Lajoie,¹⁹ Y. Le Bornec,³⁷ A. Lebedev,^{19,24} S. Leckey,⁴⁵ D.M. Lee,²⁸ M.J. Leitch,²⁸ M.A.L. Leite,⁴² X.H. Li,⁶ H. Lim,⁴³ A. Litvinenko,²⁰ M.X. Liu,²⁸ C.F. Maguire,⁵⁰ Y.I. Makdisi,⁵ A. Malakhov,²⁰ V.I. Manko,²⁴ Y. Mao,^{38,40} G. Martinez,⁴⁶ H. Masui,⁴⁹ F. Matathias,⁴⁵ T. Matsumoto,^{8,51} M.C. McCain,¹ P.L. McGaughey,²⁸ Y. Miake,⁴⁹ T.E. Miller,⁵⁰ A. Milov,⁴⁵ S. Mioduszewski,⁵ G.C. Mishra,¹⁵ J.T. Mitchell,⁵ A.K. Mohanty,⁴ D.P. Morrison,⁵ J.M. Moss,²⁸ D. Mukhopadhyay,⁵² M. Muniruzzaman,⁶ S. Nagamiya,²¹ J.L. Nagle,^{9,10} T. Nakamura,¹⁶ J. Newby,⁴⁷ A.S. Nyanin,²⁴ J. Nystrand,³⁰ E. O'Brien,⁵ C.A. Ogilvie,¹⁹ H. Ohnishi,⁴⁰ I.D. Ojha,^{3,50} H. Okada,^{25,40} K. Okada,^{40,41} A. Oskarsson,³⁰ I. Otterlund,³⁰ K. Oyama,⁸ K. Ozawa,⁸ D. Pal,⁵² A.P.T. Palounek,²⁸ V. Pantuev,⁴⁵ V. Papavassiliou,³⁵ J. Park,⁴³ W.J. Park,²³ S.F. Pate,³⁵ H. Pei,¹⁹ V. Penev,²⁰ J.-C. Peng,¹⁸ H. Pereira,¹¹ V. Peresedov,²⁰ A. Pierson,³⁴ C. Pinkenburg,⁵ R.P. Pisani,⁵ M.L. Purschke,⁵ A.K. Purwar,⁴⁵ J.M. Qualls,¹ J. Rak,¹⁹ I. Ravinovich,⁵² K.F. Read,^{36,47} M. Reuter,⁴⁵ K. Reygers,³¹ V. Riabov,³⁹ Y. Riabov,³⁹ G. Roche,²⁹ A. Romana,^{26,*} M. Rosati,¹⁹ S.S.E. Rosendahl,³⁰ P. Rosnet,²⁹ V.L. Rykov,⁴⁰ S.S. Ryu,⁵³ N. Saito,^{25,40,41} T. Sakaguchi,^{8,51} S. Sakai,⁴⁹ V. Samsonov,³⁹ L. Sanfratello,³⁴ R. Santo,³¹ H.D. Sato,^{25,40} S. Sato,^{5,49} S. Sawada,²¹ Y. Schutz,⁴⁶ V. Semenov,¹⁷ R. Seto,⁶ T.K. Shea,⁵ I. Shein,¹⁷ T.-A. Shibata,^{40,48} K. Shigaki,¹⁶ M. Shimomura,⁴⁹ A. Sickles,⁴⁵ C.L. Silva,⁴² D. Silvermyr,²⁸ K.S. Sim,²³ A. Soldatov,¹⁷ R.A. Soltz,²⁷ W.E. Sondheim,²⁸ S.P. Sorensen,⁴⁷ I.V. Sourikova,⁵ F. Staley,¹¹ P.W. Stankus,³⁶ E. Stenlund,³⁰ M. Stepanov,³⁵ A. Ster,²² S.P. Stoll,⁵ T. Sugitate,¹⁶ J.P. Sullivan,²⁸ S. Takagi,⁴⁹ E.M. Takagui,⁴² A. Taketani,^{40,41} K.H. Tanaka,²¹ Y. Tanaka,³³ K. Tanida,⁴⁰ M.J. Tannenbaum,⁵ A. Taranenko,⁴⁴ P. Tarján,¹² T.L. Thomas,³⁴ M. Togawa,^{25,40} J. Tojo,⁴⁰ H. Torii,^{25,41} R.S. Towell,¹ V.-N. Tram,²⁶ I. Tserruya,⁵² Y. Tsuchimoto,¹⁶ H. Tydesjö,³⁰ N. Tyurin,¹⁷ T.J. Uam,³² J. Velkovska,⁵ M. Velkovsky,⁴⁵ V. Veszprémi,¹² A.A. Vinogradov,²⁴ M.A. Volkov,²⁴ E. Vznuzdaev,³⁹ X.R. Wang,¹⁵ Y. Watanabe,^{40,41} S.N. White,⁵ N. Willis,³⁷ F.K. Wohn,¹⁹ C.L. Woody,⁵ W. Xie,⁶ A. Yanovich,¹⁷ S. Yokkaichi,^{40,41} G.R. Young,³⁶ I.E. Yushmanov,²⁴ W.A. Zajc,¹⁰ C. Zhang,¹⁰ S. Zhou,⁷ J. Zimányi,^{22,*} L. Zolin,²⁰ X. Zong,¹⁹ and H.W. vanHecke²⁸

(PHENIX Collaboration)

¹Abilene Christian University, Abilene, TX 79699, USA

²Institute of Physics, Academia Sinica, Taipei 11529, Taiwan

³Department of Physics, Banaras Hindu University, Varanasi 221005, India

⁴Bhabha Atomic Research Centre, Bombay 400 085, India

⁵Brookhaven National Laboratory, Upton, NY 11973-5000, USA

- ⁶University of California - Riverside, Riverside, CA 92521, USA
- ⁷China Institute of Atomic Energy (CIAE), Beijing, People's Republic of China
- ⁸Center for Nuclear Study, Graduate School of Science, University of Tokyo, 7-3-1 Hongo, Bunkyo, Tokyo 113-0033, Japan
- ⁹University of Colorado, Boulder, CO 80309, USA
- ¹⁰Columbia University, New York, NY 10027 and Nevis Laboratories, Irvington, NY 10533, USA
- ¹¹Dapnia, CEA Saclay, F-91191, Gif-sur-Yvette, France
- ¹²Debrecen University, H-4010 Debrecen, Egyetem tér 1, Hungary
- ¹³ELTE, Eötvös Loránd University, H - 1117 Budapest, Pázmány P. s. 1/A, Hungary
- ¹⁴Florida State University, Tallahassee, FL 32306, USA
- ¹⁵Georgia State University, Atlanta, GA 30303, USA
- ¹⁶Hiroshima University, Kagamiyama, Higashi-Hiroshima 739-8526, Japan
- ¹⁷IHEP Protvino, State Research Center of Russian Federation, Institute for High Energy Physics, Protvino, 142281, Russia
- ¹⁸University of Illinois at Urbana-Champaign, Urbana, IL 61801, USA
- ¹⁹Iowa State University, Ames, IA 50011, USA
- ²⁰Joint Institute for Nuclear Research, 141980 Dubna, Moscow Region, Russia
- ²¹KEK, High Energy Accelerator Research Organization, Tsukuba, Ibaraki 305-0801, Japan
- ²²KFKI Research Institute for Particle and Nuclear Physics of the Hungarian Academy of Sciences (MTA KFKI RMKI), H-1525 Budapest 114, POBox 49, Budapest, Hungary
- ²³Korea University, Seoul, 136-701, Korea
- ²⁴Russian Research Center "Kurchatov Institute", Moscow, Russia
- ²⁵Kyoto University, Kyoto 606-8502, Japan
- ²⁶Laboratoire Leprince-Ringuet, Ecole Polytechnique, CNRS-IN2P3, Route de Saclay, F-91128, Palaiseau, France
- ²⁷Lawrence Livermore National Laboratory, Livermore, CA 94550, USA
- ²⁸Los Alamos National Laboratory, Los Alamos, NM 87545, USA
- ²⁹LPC, Université Blaise Pascal, CNRS-IN2P3, Clermont-Fd, 63177 Aubiere Cedex, France
- ³⁰Department of Physics, Lund University, Box 118, SE-221 00 Lund, Sweden
- ³¹Institut für Kernphysik, University of Muenster, D-48149 Muenster, Germany
- ³²Myongji University, Yongin, Kyonggido 449-728, Korea
- ³³Nagasaki Institute of Applied Science, Nagasaki-shi, Nagasaki 851-0193, Japan
- ³⁴University of New Mexico, Albuquerque, NM 87131, USA
- ³⁵New Mexico State University, Las Cruces, NM 88003, USA
- ³⁶Oak Ridge National Laboratory, Oak Ridge, TN 37831, USA
- ³⁷IPN-Orsay, Université Paris Sud, CNRS-IN2P3, BP1, F-91406, Orsay, France
- ³⁸Peking University, Beijing, People's Republic of China
- ³⁹PNPI, Petersburg Nuclear Physics Institute, Gatchina, Leningrad region, 188300, Russia
- ⁴⁰RIKEN (The Institute of Physical and Chemical Research), Wako, Saitama 351-0198, JAPAN
- ⁴¹RIKEN BNL Research Center, Brookhaven National Laboratory, Upton, NY 11973-5000, USA
- ⁴²Universidade de S ao Paulo, Instituto de Física, Caixa Postal 66318, S ao Paulo CEP05315-970, Brazil
- ⁴³System Electronics Laboratory, Seoul National University, Seoul, South Korea
- ⁴⁴Chemistry Department, Stony Brook University, Stony Brook, SUNY, NY 11794-3400, USA
- ⁴⁵Department of Physics and Astronomy, Stony Brook University, SUNY, Stony Brook, NY 11794, USA
- ⁴⁶SUBATECH (Ecole des Mines de Nantes, CNRS-IN2P3, Université de Nantes) BP 20722 - 44307, Nantes, France
- ⁴⁷University of Tennessee, Knoxville, TN 37996, USA
- ⁴⁸Department of Physics, Tokyo Institute of Technology, Oh-okayama, Meguro, Tokyo 152-8551, Japan
- ⁴⁹Institute of Physics, University of Tsukuba, Tsukuba, Ibaraki 305, Japan
- ⁵⁰Vanderbilt University, Nashville, TN 37235, USA
- ⁵¹Waseda University, Advanced Research Institute for Science and Engineering, 17 Kikui-cho, Shinjuku-ku, Tokyo 162-0044, Japan
- ⁵²Weizmann Institute, Rehovot 76100, Israel
- ⁵³Yonsei University, IPAP, Seoul 120-749, Korea

(Dated: November 20, 2018)

We present transverse momentum (p_T) spectra of charged hadrons measured in deuteron-gold and nucleon-gold collisions at $\sqrt{s_{NN}} = 200$ GeV for four centrality classes. Nucleon-gold collisions were selected by tagging events in which a spectator nucleon was observed in one of two forward rapidity detectors. The spectra and yields were investigated as a function of the number of binary nucleon-nucleon collisions, ν , suffered by deuteron nucleons. A comparison of charged particle yields to those in $p+p$ collisions show that yield per nucleon-nucleon collision saturates with ν for high momentum particles. We also present the charged hadron to neutral pion ratios as a function of p_T .

PACS numbers: 25.75.Dw

I. INTRODUCTION

The measurement of hadron spectra at high transverse momenta (p_T) has been a powerful tool in studying the modification of particle production and propagation in the nuclear medium at the BNL Relativistic Heavy Ion Collider (RHIC). One of the most intriguing results observed so far at RHIC is the strong suppression of the yield of hadrons with p_T above ~ 2 GeV/ c in midcentral and central Au+Au collisions relative to the corresponding yield in $p+p$ collisions scaled by the sum of independent nucleon-nucleon collisions in the Au+Au interaction [1, 2, 3]. This is consistent with a picture in which the hard scattered parton loses significant energy when it traverses the medium created during the collision [4]. There is additional evidence for the strong interaction of partons with the final state medium. For example, two particle azimuthal correlations demonstrate significant modifications of jets such as width and particle content [5, 6]. In the p_T region, $2 < p_T < 5$ GeV/ c , an anomalously large baryon/meson ratio is observed [7]. The coalescence of thermal and shower partons offers a possible explanation of this phenomenon as a final state effect [8].

The hadron spectrum is sensitive to final state effects including jet quenching, parton recombination and scattering of produced particles, in addition to initial state effects, such as gluon saturation and nuclear shadowing [9], and the Cronin effect [10, 11]. If shadowing or gluon saturation are actually responsible for the large suppression seen in Au+Au collisions, these same effects would also produce a suppression of 20-30% in the yield of high p_T [9] hadrons even in d +Au collisions.

To study the role of initial state effects in the high p_T suppression, d +Au collisions at RHIC serve as a control experiment, since no dense matter is expected to be formed in these collisions. Earlier measurements on inclusive hadron production in d +Au collisions show no suppression of high p_T hadrons [12, 13]. Rather, there is a small enhancement in the yield of high momentum particles in d +Au collisions. This result implies that the effects seen in central Au+Au collisions are largely due to final state interactions in the dense medium.

In this paper, we extend our investigation of charged hadron production in d +Au collisions at $\sqrt{s_{NN}} = 200$ GeV at midrapidity with detailed centrality selections and with significantly higher statistics. The centrality selection allows one to make quantitative statements about the impact parameter dependence of particle production.

The nuclear modification of high p_T hadron production in proton reactions with heavy nuclei has previously been studied at lower center of mass energies [10, 11]. It was found that hadron yield at high p_T in $p+A$ collisions increases faster than the nuclear mass, A . This effect, known as the Cronin effect, is conventionally parametrized as A^α . At $\sqrt{s} \sim 10$ -30 GeV, α depends

on p_T and is found to be greater than unity for $p_T > 2$ GeV/ c . The exponent α also depends on the particle species; it was found to be larger for baryons than for mesons. The Cronin effect is often attributed to the multiple scattering of projectile partons propagating through the target nucleus [14].

A deuteron projectile has an additional interesting characteristic: since the average separation between the proton and neutron in the deuteron is large, on the order of few a fm, there is a class of events in which only one of the two nucleons participates in the collision. Thus d +Au events can be categorized into “ p ”+Au or “ n ”+Au collisions, when only one of the constituent nucleons interacts, and pn +Au, when both nucleons participate in the collision. In such events the interacting proton or neutron is not a free proton or neutron, so it is not exactly the same as a p +Au or n +Au interaction. For simplicity we will refer to the tagged samples as p +Au and n +Au and collectively N +Au. The selection of p +Au and n +Au collisions in the PHENIX experiment is done by tagging events where the incoming deuteron has a non-interacting neutron or proton. Combined with centrality selection, such event tagging provides better control of the collision geometry and of the number of subsequent inelastic nucleon-nucleon interactions in the gold nucleus.

Very little experimental information has been published about neutron-nucleus collisions at high energy. Tagging allows the direct comparison of pn +Au, p +Au, and n +Au interactions. Results from these collisions are compared with $p+p$ data measured by the PHENIX experiment at the same beam energy to shed light on the Cronin enhancement and other nuclear effects. Further, we have investigated the Cronin effect as a function of the number of collisions per participant nucleon in the deuteron. To estimate the fraction of pions in the charged hadron spectrum, we have looked at hadron to pion ratios as a function of transverse momentum.

The paper is organized as follows. Section II gives a detailed account of the analysis in which we describe the detector, centrality selection, charged particle background rejection, spectra corrections and systematic errors. In Sec. III, the centrality and p_T dependence of the charged hadron spectra, and a comparison with the $p+p$ and the π^0 data are discussed. A summary is given in Sec. IV.

II. EXPERIMENT AND ANALYSIS

A. Detector

The PHENIX detector consists of four spectrometer arms positioned around the vertex of colliding deuteron and gold nuclei—two central arms at midrapidity and two muon arms at forward rapidities—and a set of detectors. A detailed description of the detector can be found elsewhere, see Ref. [15] and references therein. This analysis uses the two central arms and the set of global detectors.

Each central arm covers the pseudorapidity range $|\eta| < 0.35$, and 90° in azimuth. Charged particles are tracked by drift chambers (DCs) located 2 m from the vertex and layers of pad chambers (PC1 and PC3) positioned at 2.5 and 5 m in the radial direction. The central spectrometer provides axial magnetic fields along the beam pipe. The transverse momentum, p_T of each particle is determined by its deflection angle in the azimuthal direction as measured by the DC. The total particle momentum is reconstructed by projecting tracks back to the collision vertex through the magnetic field. The track reconstruction efficiency is approximately 98% and independent of p_T with negligible centrality dependence. The particle momenta are measured with a resolution $\delta p/p = 0.007 \oplus 0.011p$, with p in GeV/ c . The absolute momentum scale is calibrated to 0.7% from the reconstructed proton mass using the PHENIX time-of-flight system. At high transverse momentum, a substantial background of electrons is produced by photon conversion in the material between the beam pipe and drift chambers. To subtract this background from photon conversion we use the ring imaging Cherenkov detector (RICH). The RICH is filled with CO₂ gas at atmospheric pressure and has a charged particle threshold $\gamma_{\text{th}} = 35$ for emission of Cherenkov photons.

To characterize the global parameters of the collision and its centrality, the PHENIX experiment uses beam-beam counters (BBCs) covering the pseudorapidity range $3.0 < |\eta| < 3.9$, zero degree calorimeters (ZDCs) and forward calorimeters (FCALs) located at $|\eta| > 6$. The locations of these global detectors are schematically shown in Fig. 1. Each BBC is an array of 64 Cherenkov counters around the beam pipe and is positioned at 1.44 m upstream or downstream of the nominal vertex location. The information from the BBC is used for the event timing, vertex position, and centrality determination. The two ZDCs are hadronic calorimeters which measure spectator neutrons [17]. They are located 18 m from the interaction point. At the top RHIC energy of 100 GeV/nucleon, neutrons evaporated from the spectator remnants of the collision are emitted within 1 mrad from the colliding beam direction. Charged fragments and the noninteracted primary beam are bent by deflecting (DX) magnets to much larger angles. The ZDC measures the total neutron energy within a small cone and with this provides the number of spectator neutrons from the interacting nucleus. The ZDC on the north side measured 100 GeV neutrons from deuteron fragmentation with a resolution of $\sigma = 28$ GeV.

The forward calorimeters were installed before the $d+Au$ run. The FCAL is a hadron calorimeter and consists of lead scintillating fiber modules originally used in BNL Alternating Gradient Synchrotron (AGS) Experiment E864 [18] rearranged into two 9 by 10 arrays. The only difference from the E864 experiment is the readout electronics, which are identical to PHENIX central arm electromagnetic calorimeter electronics. The size of each module is $10 \times 10 \times 117$ cm, the average tower density is 9.6 g/cm³, and the total length corresponds to 60 nuclear

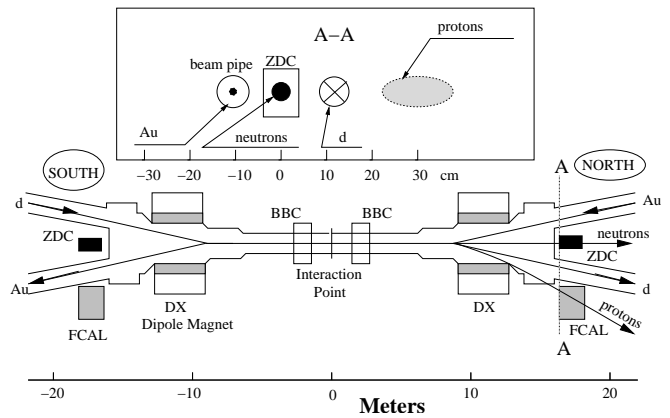


FIG. 1: FCAL, ZDC, and BBC positions relative to the vertex. The vertical scale in the figure is arbitrary. The insert at the top shows the position of primary beam, spectator neutron and proton spots at the FCAL and ZDC locations; deuteron beam, spectator neutrons and protons go into the plane, the gold beam is coming out of the plane.

interaction lengths. The two arrays are located 18 m from the interaction point along the beam pipes downstream of the first beam-line deflecting (DX) magnet. The DX magnets work as sweeping magnets for the spectator protons. The FCAL measures the energy of the spectator protons. The resolution of the FCAL on the north side for measuring 100 GeV protons from the deuteron fragmentation was $\sigma = 40$ GeV.

B. Centrality analysis

The present analysis is based on minimum bias events, defined by a coincidence of at least one photomultiplier each in the north and south BBCs. The data were taken for events with vertex position within $|z| < 30$ cm along the beam axis. A total of 6.2×10^7 events were analyzed, which corresponds to 1.6 nb^{-1} of total integrated luminosity. At this vertex cut the minimum bias trigger cross section measured by BBC is $1.99 \text{ b} \pm 5.2\%$ [19]. Thus at the trigger efficiency [12] of $88.5\% \pm 4\%$ we get the total inelastic $d+Au$ cross section of $2.26 \pm 0.1 \text{ b}$. Centrality classes in $d+Au$ events were defined by charged particle multiplicity in the BBC south (BBCS) (the gold fragmentation side). We assume that the number of charged particles firing the BBCS is linearly proportional, on average, to the number of participants from the gold nucleus in the reaction. To check this, the BBCS response was simulated as a superposition of independent N_{targ} nucleon-nucleon type reactions, where N_{targ} is the number of participating nucleons in the struck gold nucleus. As a baseline for the BBCS modeling we use unbiased data from previous RHIC $p+p$ runs where proton-proton inelastic collisions were selected with a trigger synchronized to fire whenever filled bunches crossed in the PHENIX interaction region. N_{targ} was calculated

using a Glauber model [12] with a particular parameter set [21]. The resulting distribution for minimum bias events is plotted in Fig. 2 together with experimental data.

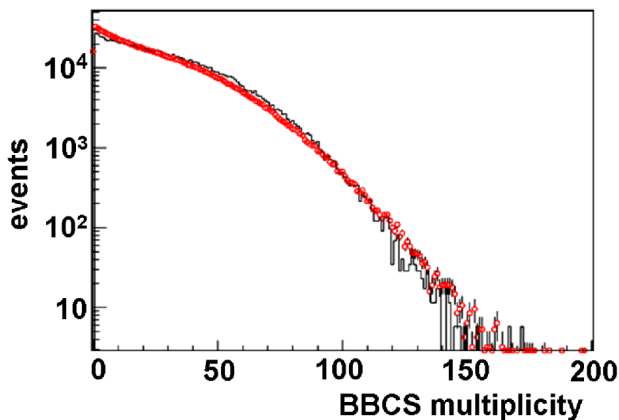


FIG. 2: (Color online) Comparison between the experimental data hit distribution in BBCS in d +Au collisions (open circles) and the calculated BBCS hit distribution (solid line).

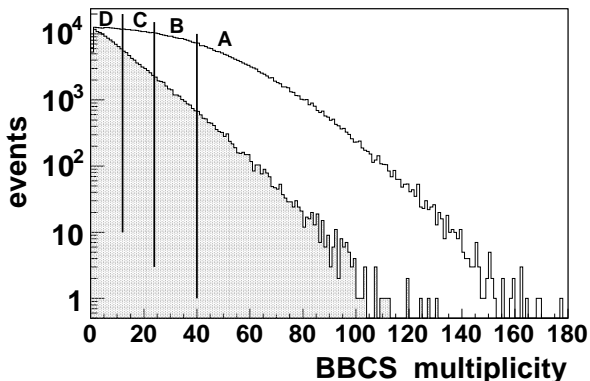


FIG. 3: Multiplicity distribution in BBCS, located on the gold nucleus fragmentation side. Four centrality classes for d +Au collisions are defined by slicing the BBCS distribution, shown with vertical lines. The same multiplicity cuts were used for the tagged sample of p +Au and n +Au events, the summed distribution of which is shown in the lower histogram.

The calculation appears to follow the general features of the data distribution, which supports our assumption that the number of BBCS firings is proportional to N_{targ} . We define four centrality classes for d +Au collisions by slicing the BBCS multiplicity distribution into four regions, A, B, C, and D (Fig. 3). These regions were selected to define in d +Au collisions four centrality classes 0–20%, 20–40%, 40–60%, and 60–88%, respectively. We have taken into account the limited trigger efficiency for

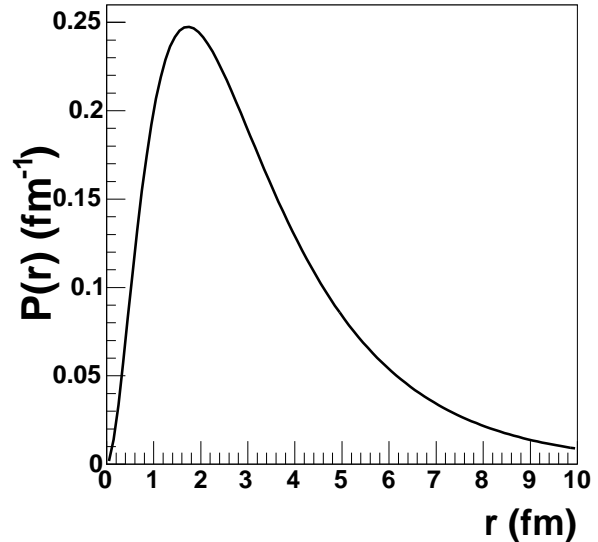


FIG. 4: Probability density distribution for the proton-neutron distance in the deuteron given by the square of the Hulthén wave function [21].

the peripheral collisions. The tagged sample, in which only one nucleon from the deuteron projectile interacts, has a differently shaped BBCS multiplicity distribution than the general data. Nevertheless, for both the tagged sample and the general data the same BBCS selections were used to define the collision centrality.

In the Glauber model Monte Carlo simulation of d +Au collisions the deuteron wave function was represented by the Hulthén form [21].¹ The square of this wave function determines the probability distribution for the proton-neutron distance in the deuteron, as shown in Fig. 4. The deuteron is a large system with a mean proton-neutron distance of about 3 fm and a significant probability to be larger. In the left side of Fig. 5, we present the calculated impact parameter distributions of d +Au collisions and the tagged N +Au sample. On the right side of Fig. 5, the corresponding distributions of the number of collisions per participant nucleon from the interacting deuteron, ν , are plotted. The parameter ν is comparable to the number of collisions suffered by the proton in p +A experiments. The impact parameter b is defined as the distance between the centers of the colliding nuclei, Au and d . This means that for the tag sample, the interaction point of participant nucleon from the deuteron is

¹ For the gold nucleus, we use the Woods-Saxon density distribution with radius $R=6.38$ fm, diffuseness parameter $a=0.54$ fm and N-N cross section $\sigma_{NN}^{\text{inel}} = 42$ mb. The deuteron is described by a Hulthén wave function with $\alpha = 0.228$ fm⁻¹ and $\beta = 1.18$ fm⁻¹, see Ref. [21].

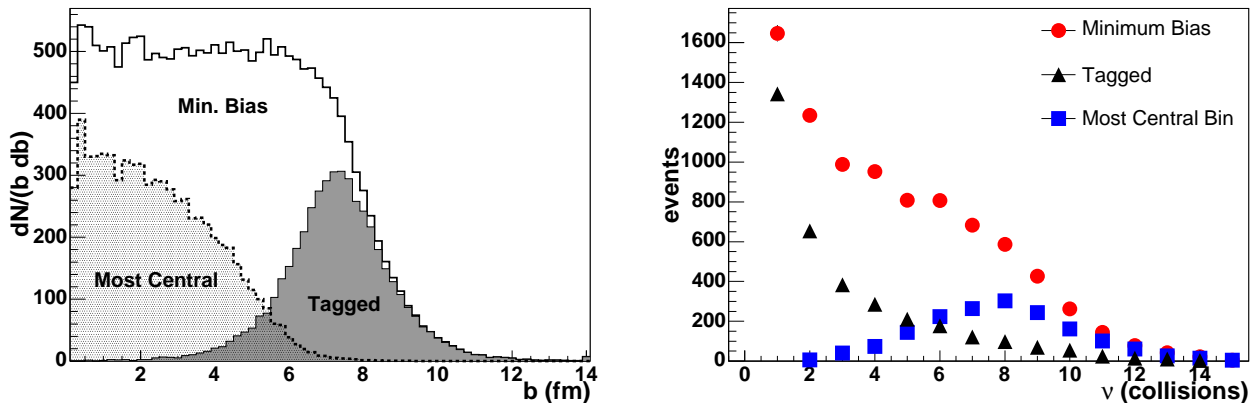


FIG. 5: (Color online) Left: impact parameter distribution for the minimum bias d +Au collisions, for the most central events (centrality bin A) and for the tagged sample. For tagged events, the impact parameter was defined from the center of the deuteron. Right: the corresponding distribution of the number of collisions per participant nucleon from deuteron, ν .

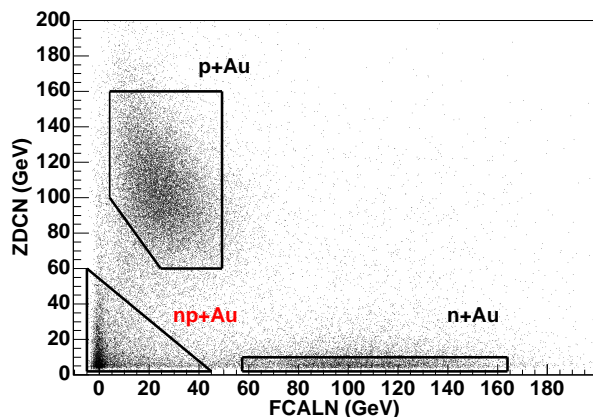


FIG. 6: (Color online) Scatter plot of ZDCN (vertical axis) and FCALN (horizontal axis) signals on the deuteron fragmentation side. Solid lines show cuts which define the p +Au and n +Au collisions.

closer to the Au center than the distance b , and the spectator nucleon leaves the interaction region at a distance larger than b . We also did a Monte Carlo simulation with the most recent deuteron wave function parametrization from Ref. [22]. We found that the difference between the calculation with the Hulthén form and the most recent parametrization for the number of nucleon collisions does not exceed 1%.

In Fig. 6 we illustrate our tag selection cuts. A p +Au collision event is tagged by the detection of a spectator neutron in the ZDC north (ZDCN) on the deuteron fragmentation side. Similarly, we use the FCAL north (FCALN) on the deuteron fragmentation side to detect a spectator proton and thereby tag n +Au collision events. The scatter plot in Fig. 6 shows the ZDCN and FCALN signals and has three distinct regions. Region 1 is defined as small or no signal in both the ZDCN and FCALN,

which corresponds to the case in which both nucleons from the deuteron interact with the Au nucleus. Region 2 has a small signal in the ZDCN and about 100 GeV amplitude signal in the FCALN. This corresponds to tagged n +Au collisions. Region 3 has a small signal in the FCALN and about 100 GeV energy release in the ZDCN. Events in this region are tagged p +Au events. In Region 3, there is a small (anti) correlation between the ZDCN and FCALN. The reason for this is the close proximity of the FCALN to the ZDCN, see Fig. 1. The ZDCN effectively acts as a secondary target for 100 GeV spectator neutrons. There is some contamination of secondary particles produced in the ZDCN into the large volume FCALN.

The purity of the tag samples from possible background contamination was thoroughly investigated. Figure 7 shows ZDCN and FCALN responses for the most central events. Background may contribute to the tag sample from the left side of the spectrum with low amplitudes. To estimate the background contamination we fitted the left part of the spectrum using an exponentially falling function and fitted a Gaussian function to the detector response to the spectator nucleon. The thin smooth line in Fig. 7 shows the sum of the two functions. The background under the Gaussian peak was estimated as the integral of the exponential function above our cut, which is marked by the vertical line and arrow. In central p +Au events we estimate 2.8% contamination in the ZDCN spectrum. For more peripheral events this contamination decreases and reaches 1.4% in the most peripheral bin.

The background contamination in the FCALN defined n +Au sample is more complicated. For the most central events, as shown in Fig. 7 on the right, the background contributes 0.4% to the area above our cut. As centrality changes so too does the shape of the background spectrum. Figure 8 illustrates the problem of background estimation. Attempts to fit the background spectrum with

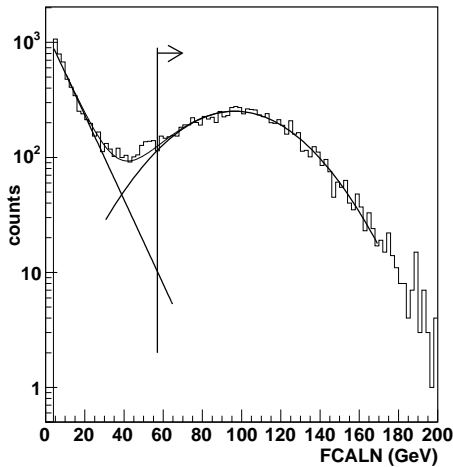
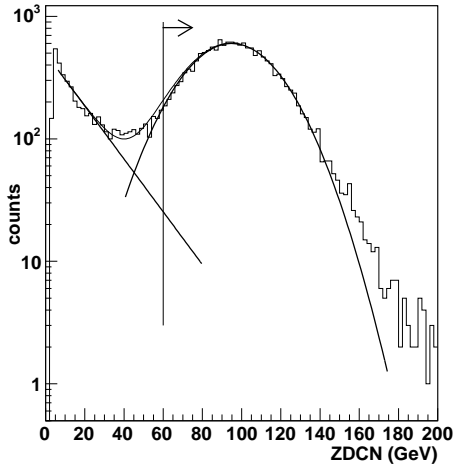


FIG. 7: ZDCN and FCALN spectra for the most central tagged events. Detector response to the spectator nucleon is fit with a Gauss function. Background from the left side of the spectra was fit to an exponential function and extrapolated to the region above our cuts. All events to the right of the cuts, shown by vertical solid lines, were defined as a tag sample.

an exponential function, as was done for central events, failed. The sum of the estimated background and the Gauss fit is well above the experimental data implying that the background spectrum falls much faster than a simple exponential function. However, the relevant question in assessing the background contamination is not its absolute or relative value, but rather how much it could distort our experimental data. The goal of this analysis is to measure the charged hadron spectrum in the PHENIX central arms. Thus, we can estimate the stability of our results measured by the central arms versus different cuts applied to the FCALN. We define the stability of the measurement, S , in a particular FCALN bin (Fig. 9) as the ratio of the number of charged particle tracks per event with $p_T > 0.5 \text{ GeV}/c$ for this cut to a reference cut

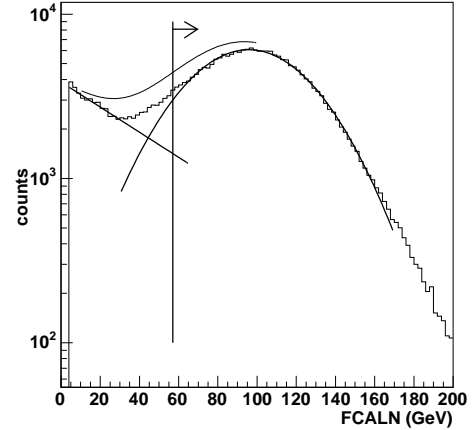


FIG. 8: FCALN spectrum for the most peripheral tagged events, with the same line notation as Fig. 7. The plot illustrates the difficulty of evaluating the background contribution in the most peripheral collisions: background fit with an exponentially falling spectrum significantly overestimates the contribution to the events above our cut.

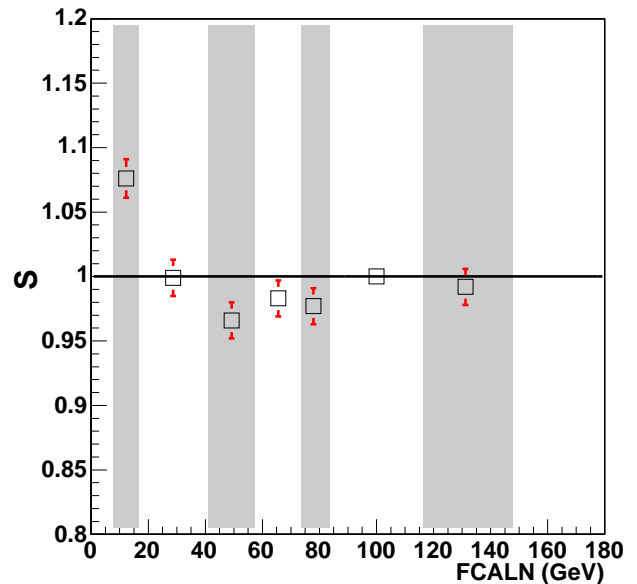


FIG. 9: (Color online) Stability of the results for different FCALN bins, see text for details.

in which the signal to background ratio is the largest. For the reference cut we use $100 \pm 20 \text{ GeV}$ FCALN response (within region 3 as defined above). This is the most probable detector response for a spectator proton as seen in Fig. 8. We observe that in the region just to the left of our reference cut, where we may expect about equal amount of signal and background events, the parameter S is only 3% smaller than unity, as seen in Fig. 9. Within errors, S does not depend on track momentum.

Thus, in the worst case the background contamination effect is less than 2% for events above our cut in the n +Au tagged sample.

We do not correct the tagged sample results for any contamination. We average the two tagged samples to form a single nucleon + Au (N +Au) sample.

For each of the four BBCS multiplicity regions shown in Fig. 3, using a Monte Carlo model within the Glauber multiple collision formalism [23], we calculate for the d +Au and the tagged N +Au collisions the average number of participating nucleons N_{part} , the nuclear overlap function T_{AB} , the number of collisions N_{coll} , and number of collisions per participant nucleon from the deuteron ν . The calculated values are presented in Table I. The nuclear overlap function T_{AB} is defined as

$$T_{AB}(b) = \int d^2 \vec{s} T_A(\vec{s}) T_B(|\vec{b} - \vec{s}|), \quad (1)$$

where the integration is performed over the element of overlapping area $d^2 \vec{s}$, and $\vec{s} = (x, y)$ is a vector in the transverse plane of interacting nuclei at the impact parameter \vec{b} between the centers of the nuclei. For nucleus A the nuclear thickness function $T_A(b)$ is defined as

$$T_A(b) = \int dz \rho_A(b, z). \quad (2)$$

TABLE I: Total number of participants N_{part} , number of collisions N_{coll} , nuclear overlap function T_{AB} , see Eq. 10, average number of collisions per participant nucleon from deuteron ν , and the BBC bin correction factor for different centrality classes.

Cent. bin	$\langle N_{\text{part}} \rangle$	$\langle N_{\text{coll}} \rangle$	$\langle T_{AB} \rangle, \text{mb}^{-1}$	ν	C_{BBC}
A	15.0±1.0	15.4±1.0	0.37±0.02	7.5±0.5	0.95±0.03
B	10.4±0.4	10.6±0.7	0.25±0.02	5.6±0.4	0.99±0.01
C	7.0±0.6	7.0±0.6	0.17±0.01	4.0±0.3	1.03±0.01
D	3.2±0.3	3.1±0.3	0.07±0.01	2.2±0.2	1.04±0.03
tag A	10.6±0.7	9.6±0.7	0.23±0.02	9.6±0.7	0.93±0.03
tag B	8.0±0.6	7.0±0.6	0.17±0.02	7.0±0.6	0.95±0.02
tag C	5.6±0.3	4.6 ±0.3	0.11±0.01	4.6±0.3	0.95±0.02
tag D	3.1±0.2	2.1±0.2	0.05±0.01	2.1±0.2	0.97±0.04

Normalization of $T_{AB}(b)$ is done by integration over all impact parameters:

$$\int d^2 b T_{AB}(b) = A B. \quad (3)$$

The average number of binary inelastic nucleon-nucleon collisions at impact parameter b was calculated from $T_{AB}(b)$ as

$$\langle N_{\text{coll}} \rangle = \sigma_{NN} T_{AB}(b), \quad (4)$$

where σ_{NN} is the inelastic nucleon-nucleon cross section [21].

An additional multiplicative correction factor, C_{BBC} , see Table I, has been applied to the data for different centrality bin selections [20]. This correction addresses two

effects, each of which distorts the centrality classification in the opposite direction. Because of natural fluctuations in the number of produced charged particles at a particular impact parameter, the BBCS centrality selections have imperfect resolution. In the case of a steeply falling BBCS multiplicity spectrum, especially for the tagged sample (see Fig. 3), there is a contamination of peripheral collision events into a more central event class. This effectively decreases the actual number of N_{coll} and particle production in the central events. The second effect is due to the BBC coincidence required for a PHENIX event trigger. In all calculations we used for the inelastic nucleon-nucleon cross section $\sigma_{NN} = 42$ mb. Actually, this cross section has three components: nondiffractive collisions with 28 mb, single diffractive collisions with 10 mb, and double diffractive collisions with 4 mb cross section [24]. From Monte Carlo simulation of $p+p$ collisions we found BBC trigger efficiencies of about $(72 \pm 1)\%$, $(7 \pm 1)\%$ and $(32 \pm 1)\%$, for each process respectively. In the Monte Carlo simulation we use the PYTHIA 6.2 event generator [24] and the GEANT simulation of the BBC detector. Single and double diffractive collisions produce particles dominantly near the beam rapidity and thus have a small probability for particle production in the BBC acceptance of $3.0 < |\eta| < 3.9$, and an even smaller probability at midrapidity. Therefore, the BBC trigger is biased to the nondiffractive collisions, which have larger particle production at midrapidity. In more central events as the number of nucleon-nucleon collisions increases the probability that there will be at least one nondiffractive collision approaches 100%; thus the BBC bias becomes negligible in central events.

C. Charged hadron analysis

The present analysis follows the methods of the analysis described in Ref. [3]. The majority of background tracks are particles with low momenta, which in traveling from DC to PC3 undergo multiple scattering and are additionally deflected in the residual magnetic field behind the DC.

To minimize this background we employ a track matching cut in the PC3 that rejects tracks whose displacement in the ϕ or z direction, D_ϕ and D_z , respectively, is greater than 2.5 standard deviations. In addition we make a fiducial cut around the z vertex determined by the BBC. Despite these veto cuts, there is still significant background contamination for p_T above 4 GeV/ c which must be subtracted. The main sources of the remaining background are e^+e^- pairs from photon conversions in the material between the collision vertex and the drift chamber, and secondary particles produced by hadron decays.

To distinguish these backgrounds, we use the RICH detector to divide all tracks into two subsets: tracks with an associated RICH signal, N_R , and tracks with no signal in the RICH, N_{NR} . Tracks with at least one hit in the RICH contain high p_T pions and conversion electrons. For re-

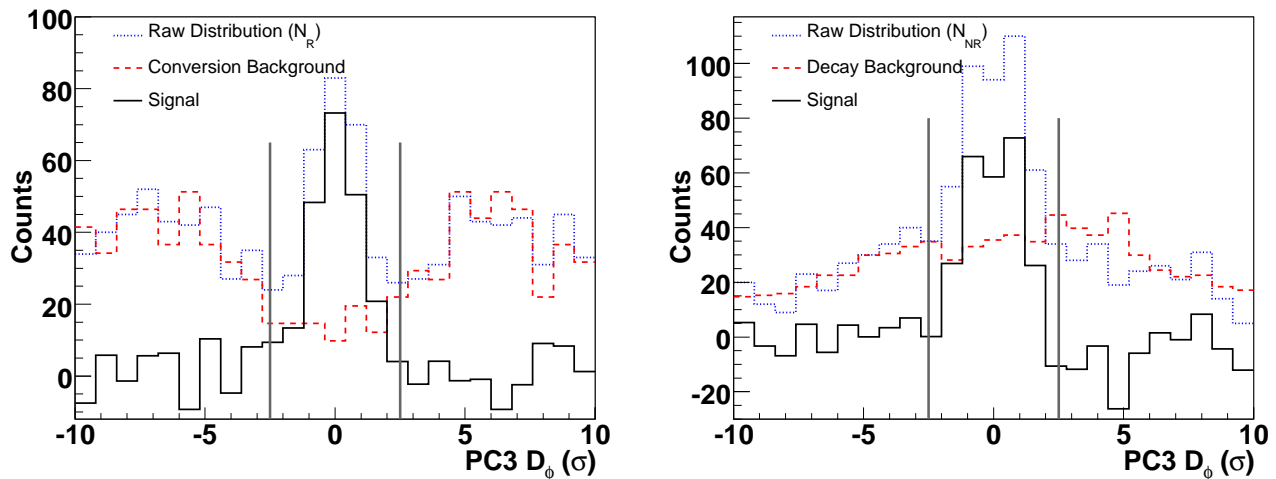


FIG. 10: (Color online) PC3 D_ϕ distributions for the conversion subtraction (left) and the decay subtraction (right) shown for minimum bias with $6 < p_T < 7$ GeV/ c . The raw distributions, N_R and N_{NR} for conversion and decay respectively, are shown with dotted lines. The estimated conversion background shown with a dashed line is N_e/R_e . The estimated decay background, shown with a dashed line, was obtained by scaling the PC3 distribution of N_{NR} tracks with $p_T > 10.5$ GeV/ c based on the ($4\sigma < |D_\phi| < 10\sigma$) region. In both plots, the signal is the raw minus the estimated background distributions. The vertical bars show the track matching cuts at $\pm 2.5 D_\phi$.

constructed electrons with momentum above 150 MeV/ c , the average number of photomultiplier tube (PMT) hits in the RICH associated with the track is $\langle N_{\text{PMT}} \rangle \approx 4.5$.

The RICH detects more than 99% of all conversion electrons for $N_{\text{PMT}} \geq 1$. At this threshold the RICH also detects pions with $p_T \geq 4.8$ GeV/ c , but the number of associated PMTs for pions reaches its asymptotic value well above 10 GeV/ c ; for a 10 GeV/ c pion $\langle N_{\text{PMT}} \rangle = 3.6$. Therefore we label tracks with $N_{\text{PMT}} \geq 5$ as electron tracks, N_e , which compose some fraction, R_e , of conversion electrons. To calculate this fraction, we take advantage of the deflection of conversion electrons in the magnetic field between the DC and PC3. This deflection leads to poor track matching in PC3 which distinguishes electrons from true high p_T pions. We define poor PC3 track matching as a displacement of more than four standard deviations in the ϕ direction. Thus we measure the value of R_e as the fraction of N_R with $4\sigma < |D_\phi| < 10\sigma$. For minimum bias events we find $R_e = 0.41 \pm 0.01$. The real pion signal S_R in the N_R sample, is calculated for each p_T bin as

$$S_R = N_R - \frac{N_e}{R_e} \quad (5)$$

The PC3 distribution for the conversion subtraction is shown on the left side of Fig. 10. The conversion subtraction is performed independently in each centrality bin. The definition of N_e (tracks with $N_{\text{PMT}} \geq 5$) does not perfectly select electron tracks, as some fraction of pions satisfies the cut. This leads to a fraction of authentic pions, which have $N_{\text{PMT}} \geq 5$, being subtracted along with the conversion electrons. This fraction is small below 7 GeV/ c , but increases rapidly for higher p_T . We calculate a correction factor to address this over-subtraction,

using a Monte Carlo simulation of the detector. The uncertainty associated with this correction, $\delta_{\pi \text{ loss}}$, is shown later in Table III.

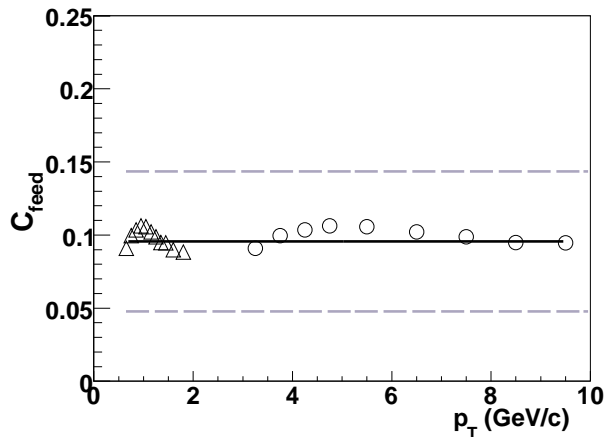


FIG. 11: Feed-down contamination as the ratio of protons and charged pions from feed-down decays to total detected charged hadrons. The low p_T points shown with triangles are calculated using the fraction of $p + K$ particles to hadrons measured in Ref. [26]. The higher p_T points are calculated using the various ratios of Eq. 8. The solid line is a fit to both sets of points and is used as C_{feed} . It is bracketed by dashed lines showing the assigned 50% systematic uncertainty.

The N +Au sample is averaged over p +Au and n +Au events. This is based on the good agreement between the yields of the two tagged samples, as shown in Fig. 13.

The hadron decay background is of two types: “decay” and “feed down.” The decay background is produced by π and K decays far from the source and thus with re-

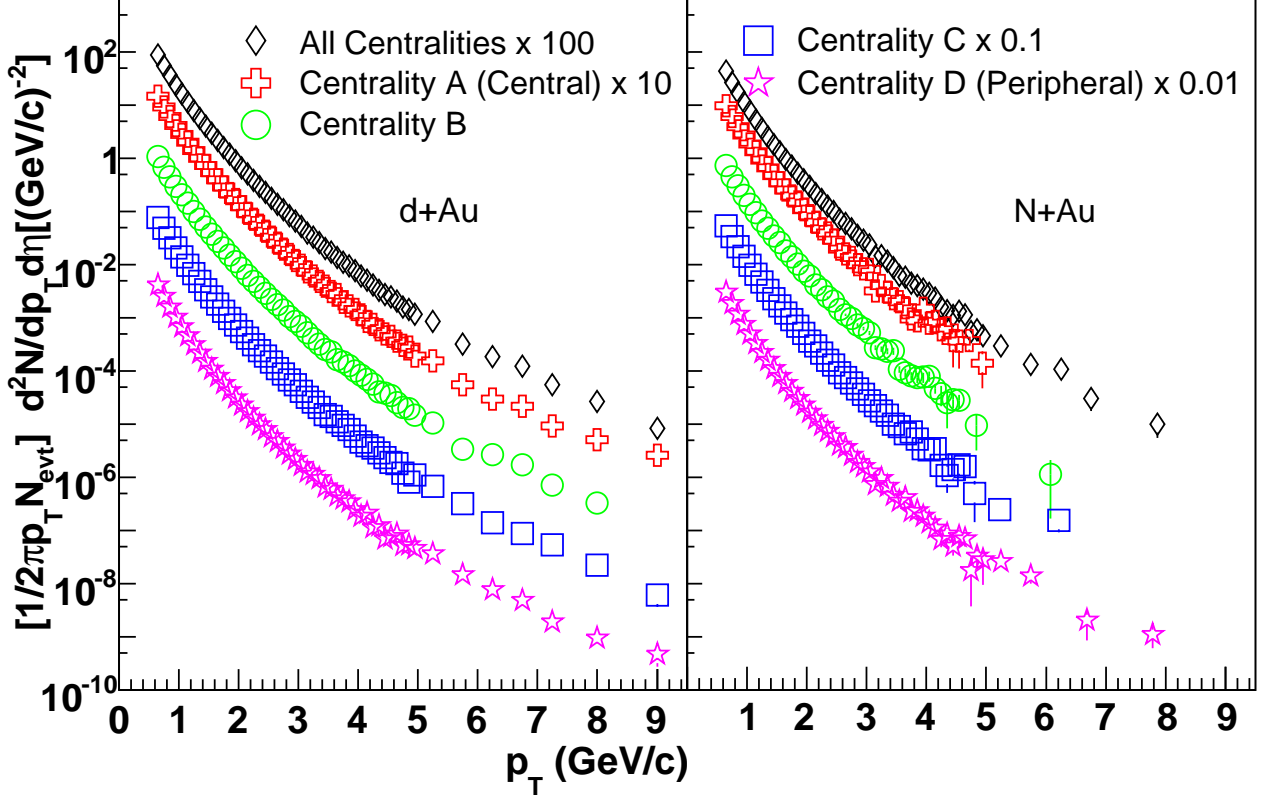


FIG. 12: (Color online) Charged hadron spectra for centrality selected $d+Au$ collisions and $N+Au$ collisions. The error bars represent statistical uncertainties only, although they are generally smaller than the data point symbols. Points from different centrality bins are scaled sequentially by a factor of 10. (See Table I for centrality class definitions.)

constructed momenta different from their true momenta, whereas the feed-down background is produced by weak decays of short-lived particles, mostly K_s^0 and Λ particles near the event vertex with apparent momenta close to their true momenta.

From tracks with no RICH signal, the N_{NR} sample, we define a subsample by selecting tracks with $p_T > 10.5 \text{ GeV}/c$, a p_T region which is almost exclusively background. We expect that its shape in D_ϕ will be the same as the background in the lower p_T region. Within this subsample we calculate the ratio, R_{decay} , of tracks which pass the PC3 cut ($|D_\phi| < 2.5\sigma$) to those with a poor match ($4\sigma < |D_\phi| < 10\sigma$). For minimum bias events $R_{\text{decay}} = 0.55 \pm 0.03$. For each momentum bin, the total decay background is then obtained by multiplying the N_{NR} tracks with poor PC3 matching ($4\sigma < |D_\phi| < 10\sigma$) by R_{decay} . The PC3 distribution for the decay subtraction is shown on the right side of Fig. 10. The decay background as a function of p_T is measured and subtracted independently in each centrality bin.

The feed-down subtraction addresses the detected π and p particles that were produced in the decays of K_s^0

and Λ particles, so we define the total feed-down contamination as:

$$C_{\text{feed}} = \frac{(p + \pi)^{\text{feed}}}{h^{\text{detected}}} \quad (6)$$

averaging over charged particle and antiparticle yields. For feed-down estimation, we have no statistical recourse and must resort to simulation to find the contamination. We assume that the spectral shapes of the K_s^0 and Λ follow the shapes of the charged kaon and proton spectra, respectively. There is good agreement of Monte Carlo simulations in $d+Au$ [26] and minimum bias Au+Au [3] for proton feed down. We therefore use the Au+Au Monte Carlo simulation, which also includes K_s^0 to pion processes, to obtain the ratio $(p + \pi)^{\text{feed}} / (p + K)^{\text{detected}} = 0.2$, after the decay background subtraction. To make use of this ratio we rewrite the contamination as:

$$C_{\text{feed}} = \frac{(p + \pi)^{\text{feed}}}{(p + K)^{\text{detected}}} \frac{(p + K)^{\text{detected}}}{h^{\text{detected}}} \quad (7)$$

To find the contamination we use the fraction of $p + K$ particles in our measured hadron sample. To do so, for

p_T less than 2.5 GeV/c we use the PHENIX published data on identified hadron production in $d+Au$ [26]. We explicitly calculate the $(p+K)^{\text{detected}}/h^{\text{detected}}$ ratio from those data. At higher p_T assuming π^0 has the same yield as π^\pm , we subdivide this ratio as

$$\frac{p+K}{h} = \frac{p+K}{\pi} \frac{\pi}{h} = \left(\frac{p}{\pi} + \frac{K}{\pi^0} \right) \frac{\pi^0}{h} \quad (8)$$

so that the right-hand side consists of all measured quantities. The p/π ratio is taken from STAR measurements [27] scaled to match the PHENIX data [26] in their common p_T region. The K/π^0 ratio is calculated from Refs. [12] and [25]. The ratio of π^0 s to hadrons is calculated from the charged hadron measurement of this analysis and π^0 measurements in Ref. [12]. From both the low and high p_T regions C_{feed} is calculated to be 9.6%. To this factor we assign a 50% systematic uncertainty based on uncertainty of the various particle ratios and the Monte Carlo simulation. C_{feed} is shown in Fig. 11. We correct for the effects of feed-down decay by multiplying the spectra remaining after the conversion and decay subtraction by $1 - C_{\text{feed}}$.

Following the background subtraction, we constructed a single, p_T dependent correction function to correct the hadron spectra for acceptance, decay in flight, reconstruction efficiency, and momentum resolution. The correction is determined by using a Monte Carlo simulation [16] of the PHENIX detector. The correction function is necessarily particle species dependent to take into account multiple scattering and decays, therefore we calculate separate correction functions for π^+ , π^- , K^+ , K^- , p^+ , and p^- . The individual functions are weighted by the particle p_T spectra measured in peripheral Au+Au collisions [28] to form a single correction factor, $C_{\text{MC}}(p_T)$, subject to a systematic uncertainty, δ_{MCweight} , stemming from uncertainty on the particle mixture [12]. For absolute normalization of the spectra we match the geometrical acceptance of the Monte Carlo simulation with the actual acceptance of the data. To obtain the charged hadron yield we multiply the background-subtracted spectra by the correction function. We normalize each centrality bin by dividing by the number of events, and each momentum bin by dividing by its bin width. Each data point is corrected so its value corresponds to the bin center. We define the invariant hadron yield as

$$\frac{1}{N_{\text{evt}}} \frac{d^2 N}{2\pi p_T dp_T d\eta} = \left(\frac{d^2 N}{2\pi p_T dp_T d\eta} \right)^{\text{bkg-subtracted}} \frac{1}{N_{\text{evt}}} (1 - C_{\text{feed}}) C_{\text{MC}}(p_T) C_{\text{BBC}} \quad (9)$$

All of the preceding steps are applied to the tagged $N+Au$ (nucleon + gold) sample as well as to the general $d+Au$ sample.

We further examine the $d+Au$ invariant yields by comparing them with the invariant yield from $p+p$ collisions.

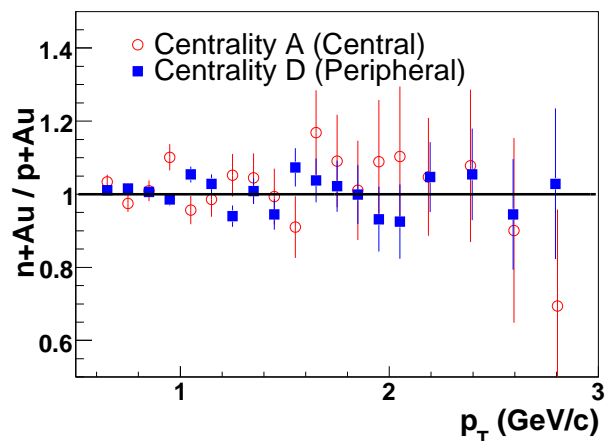


FIG. 13: (Color online) Ratio of $n+Au$ to $p+Au$ invariant yield per event shown in the most central and peripheral bins. The error bars are statistical only, as all systematic uncertainties cancel in the ratio. (See Table I for centrality class definitions.)

Previous experiments have demonstrated suppression of charged hadron and pion yields in Au+Au collisions [3]; such suppression can be quantified by the nuclear modification factor R_{AB} . For any collision of nuclei $A+B$, R_{AB} is calculated for each centrality class as the ratio of the yield in $A+B$ collision to the cross section in $p+p$ collisions scaled by the nuclear overlap function $\langle T_{AB} \rangle$, that is,

$$R_{AB}(p_T) = \frac{(1/N_{\text{evt}}) d^2 N^{A+B}/dp_T d\eta}{\langle T_{AB} \rangle d^2 \sigma^{p+p}/dp_T d\eta}. \quad (10)$$

$\langle T_{AB} \rangle$ is determined by the density distribution in the nuclei A and B and is averaged over the impact parameter range within a particular centrality class. In our case, nucleus A refers to the deuteron (or the single nucleon in tagged events), and nucleus B refers to the gold nucleus. $\langle T_{AB} \rangle$ values are presented in Table I. Using the PHENIX $p+p$ spectra [29], we thus calculate R_{dAu} and R_{NAu} .

TABLE II: Systematic uncertainties that are constant for all p_T .

Source	Uncertainty (%)
Geometric acceptance correction	2.9
Track matching	2.2
Run-by-run variation	5
Feed-down correction	4.8
δ_{MCweight}	3.7
Total	8.7

We estimate systematic uncertainties in the methods and assumptions of our analysis as displayed in Tables II and III. Table II shows uncertainties in the spectra that

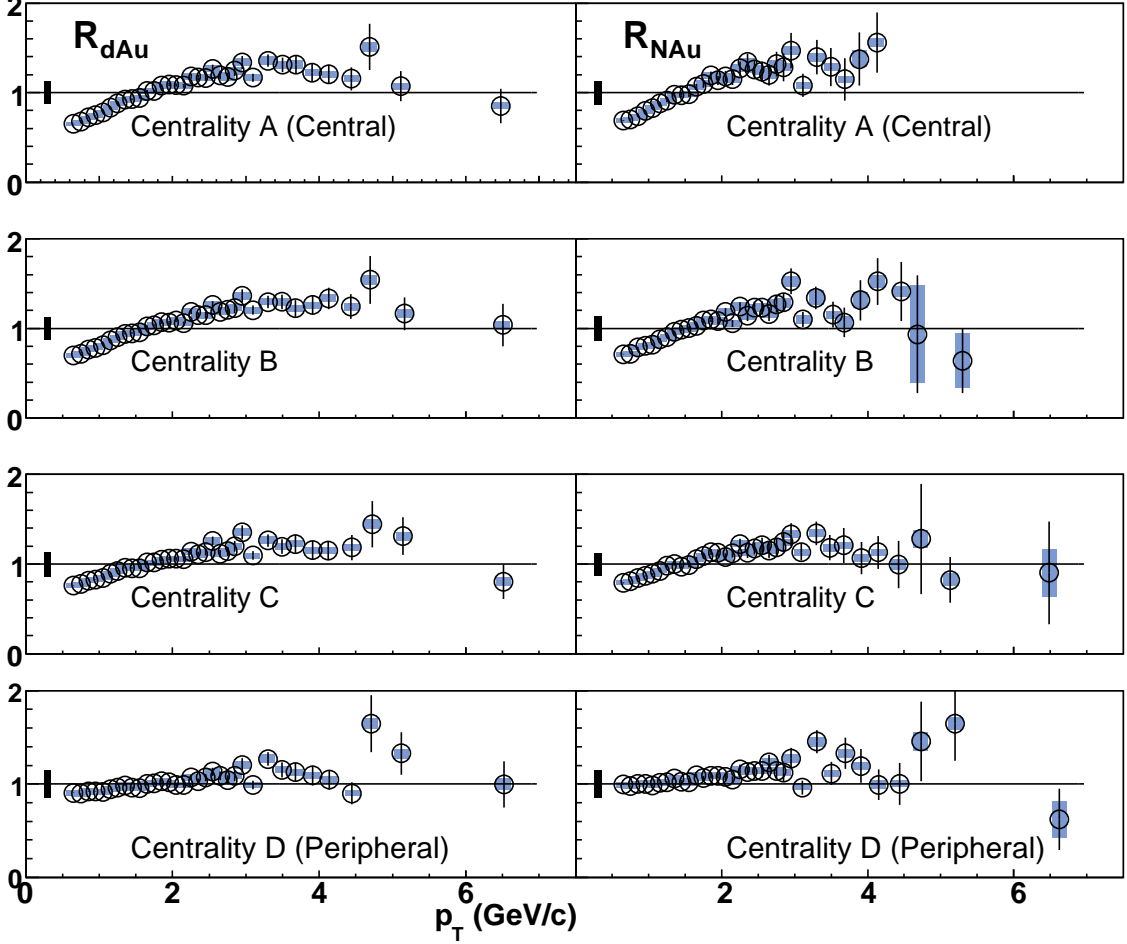


FIG. 14: (Color online) From left to right: R_{dAu} , R_{NAu} as functions of p_T . The bars represent statistical uncertainty (often smaller than the data point symbols), the shaded boxes on each point represent systematic uncertainties that change with p_T , and the black boxes on the left show systematic uncertainties that do not change with p_T . (See Table I for centrality class definitions.)

TABLE III: Systematic uncertainties that vary with p_T . Background subtraction (Bckg. sub.) uncertainties refers to the 0–88% $d+Au$ spectra; the uncertainties are greater in the more peripheral $d+Au$ and more central $N+Au$ spectra.

p_T (GeV/c)	Mom. res. (%)	Mom. scale (%)	Bckg. sub. (%)	$\delta_{\pi\text{loss}}$ (%)	Total (%)
<4.5	<0.5	<3.2	<0.1	<0.3	<3.3
4.5–5.5	<0.6	3.3	0.5	0.5	3.4
5.5–6.5	0.8	3.5	1.4	1.1	4.0
6.5–7.5	1.0	3.6	2.0	3.6	5.6
7.5–8.5	1.4	3.7	4.9	6.9	9.3
8.5–9.5	1.8	3.8	11.9	13.9	18.8

do not vary with p_T , and Table III shows uncertainties that vary with p_T . All the uncertainties listed in Table II propagate into the R_{AB} and the hadron/ π^0 ratio,

although the uncertainty from the feed-down correction partially cancels in the R_{AB} because of an analogous uncertainty in the $p + p$ reference spectrum. The background subtraction and momentum scale uncertainties only partially cancel in the R_{AB} ; the momentum resolution uncertainty and $\delta_{\pi\text{loss}}$ fully cancel. The $p + p$ reference spectrum also introduces an uncertainty that ranges from 10.7% in the low p_T bins to 11.3% at $p_T > 2$ GeV/c. The π^0 analysis [13] we used in the hadron/ π^0 ratios applies the same BBC bias correction factors as the present analysis and therefore the uncertainty stemming from this correction factor is canceled.

III. RESULTS

The fully corrected p_T distributions of $(h^+ + h^-)/2$ for $d+Au$ and $N+Au$ collisions for minimum bias and four centrality classes are shown in Fig. 12. The $d+Au$ data

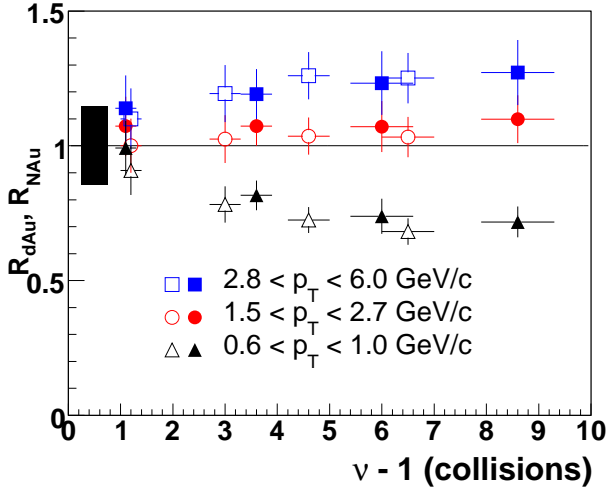


FIG. 15: (Color online) R_{dAu} (open symbols) and R_{NAu} (closed symbols) values averaged in three momentum ranges as functions of $\nu - 1$. Point-by-point uncertainty bars show the quadratic sum of the statistical uncertainty in R_{AB} and the systematic uncertainties that change with ν . The box on the far left represents the size of the systematic uncertainty that does not change with ν . Horizontal bars show the uncertainty in the value of ν for each centrality class.

are in good agreement with the sum of identified hadrons published in Ref. [26].

Figure 14 shows R_{dAu} and R_{NAu} . As expected, in the most peripheral $N+Au$ bin, with $N_{\text{coll}} = 2.1$, R_{NAu} is consistent with unity. R_{dAu} and R_{NAu} are in agreement within our uncertainty bounds.

The enhancement of the hadron yield relative to $p + p$ collisions has previously been observed in lower energy $p+A$ collisions [10, 11], and is called the Cronin effect. We observe that R_{dAu} and R_{NAu} are systematically larger than unity in the momentum range between 1.5 GeV/c and 5 GeV/c with maximum amplitude around 1.3.

There are many theoretical models with very different assumptions about initial state effects, which describe the Cronin effect [30, 31, 32, 33]. All the models agree that there is at least one additional scattering of the initial nucleon or parton while propagating through the target nucleus. This scattering increases the intrinsic transverse momentum of the colliding parton, and leads to a broadening of the parton p_T distribution. We can parametrize the effect of this broadening by writing the mean value of parton intrinsic momentum k_T as

$$\langle k_T^2 \rangle_{pA} = \langle k_T^2 \rangle_{pp} + \langle k_T^2 \rangle_A, \quad (11)$$

where $\langle k_T^2 \rangle_{pp}$ is the square of the initial parton transverse momentum in the proton, $\langle k_T^2 \rangle_A$ is an additional momentum squared after rescattering, and $\langle k_T^2 \rangle_{pA}$ is the final broadened width. Most of the models differ on the assumption they use to describe $\langle k_T^2 \rangle_A$: whether there is a single hard scattering [32] or a sum of small sequential rescatterings [31] that produces the additional k_T .

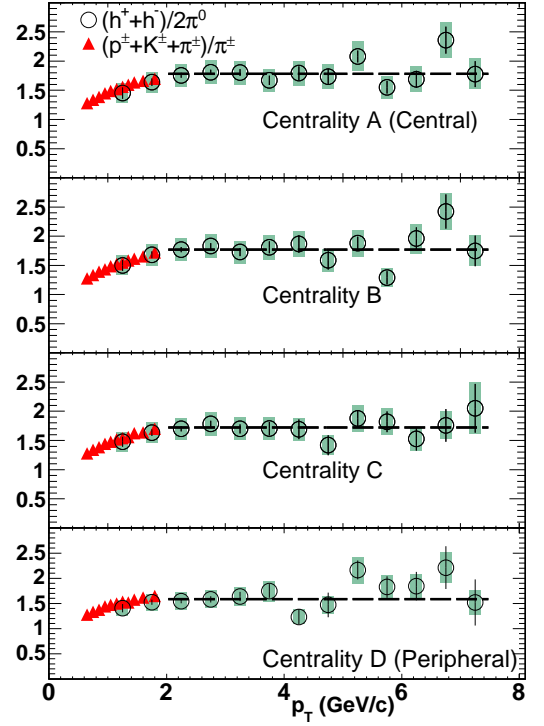


FIG. 16: (Color online) $(h^+ + h^-)/2\pi^0$ ratios as functions of transverse momentum from $d+Au$ collisions in four centrality bins. Open circles are the charged hadron spectra from the present analysis divided by π^0 data from Ref. [13]. Bars indicate statistical uncertainties, and the shaded boxes systematic uncertainties. Triangles are the $(p^\pm + K^\pm + \pi^\pm)/\pi^\pm$ ratios from Ref. [26], with statistical uncertainties roughly the size of the symbols. (See Table I for centrality class definitions.)

Common to the models is that $\langle k_T^2 \rangle_A$ is a function of the number of sequential nucleon-nucleon collisions, ν . For impact parameter b , $\langle k_T^2 \rangle_A$ can be written as:

$$\langle k_T^2 \rangle_A(b) = H(\nu(b) - 1), \quad (12)$$

where H is the square of the average momentum acquired in $\nu - 1$ rescatterings. For a single hard scattering model, $\langle k_T^2 \rangle_A$ should saturate at $\nu = 2$. We therefore investigate the shape of R_{dAu} as a function of ν to illuminate the underlying process. The centrality selection of our data and the tagged $N+Au$ sample allow us to investigate precisely the effect of the collision geometry. We use $\nu = \langle N_{\text{coll}}/N_{\text{part}}^{\text{deuteron}} \rangle$ (in $N+Au$ collisions $\nu = \langle N_{\text{coll}} \rangle$) to look explicitly at the impact parameter dependence of the nuclear modification factor.

In Fig. 15, we plot R_{dAu} and R_{NAu} as a function of $(\nu - 1)$. The values of ν are presented in Table I.

Three transverse momentum regions were selected to study the dependence of R_{AB} on ν : $2.8 \leq p_T \leq 6.0$, $1.5 \leq p_T \leq 2.7$, and $0.6 \leq p_T \leq 1.0$ GeV/c. In the low p_T region, we expect scaling with the number of participating nucleons rather than with the number of binary collisions; therefore R_{AB} is less than unity. The Cronin effect is observed in the $2.8 \leq p_T \leq 6.0$ GeV/c region, where

within the limits of our uncertainties, it is independent of the number of additional scatterings ($\nu - 1$). In the intermediate p_T region, the data show little to no Cronin enhancement, thus confirming scaling with the number of binary collisions. Just as $R_{dAu}(p_T)$ and $R_{NAu}(p_T)$ matched very closely, so do $R_{dAu}(\nu)$ and $R_{NAu}(\nu)$.

As discussed above, previous experiments found a larger Cronin enhancement for protons than pions [11]. Recently the PHENIX Collaboration published identified pion, kaon, and proton production data from $\sqrt{s_{NN}} = 200$ GeV $d+Au$ collisions [26], in which a similar Cronin behavior was observed. R_{dAu} for protons reaches about 1.8 at $p_T \approx 3$ GeV/ c , whereas pion R_{dAu} is measured to be about 1.1 for transverse momentum between 2 and 2.6 GeV/ c .

At the time these data were taken, the PHENIX experiment did not have the capability to measure identified charged pions and protons at momenta above 2.6 GeV/ c and 4 GeV/ c , respectively. To extend the trends observed in these low momentum regions [26], we calculate the ratio of the charged hadrons measured in the present analysis to the π^0 spectra from Ref. [13], alongside the ratio of $(p^\pm + K^\pm + \pi^\pm)/\pi^\pm$ from [26]. These ratios are presented in Fig. 16.

In the transverse momentum region common to the two presented ratios there is strong agreement between the analyses. The $(h^+ + h^-)/2\pi^0$ ratio is independent of p_T above 2 GeV/ c where the identified particle data end, implying that the R_{dAu} and particle ratio trends observed at low transverse momentum continue at higher transverse momentum. The average value of 1.58 ± 0.03 of the $(h^+ + h^-)/2\pi^0$ ratio for p_T above 2 GeV/ c in the peripheral D centrality bin agrees well with the value of 1.59 obtained from lower energy collisions in the CERN Intersecting Storage Rings (ISR) [34]. As found in Ref. [1] for Au+Au collisions, this value rises for more central events: we find average values of 1.78 ± 0.02 , 1.77 ± 0.03 , and 1.72 ± 0.03 for centrality bins A, B, and C, respectively. There is an additional 11% systematic uncertainty common to all four values. The centrality dependence implies moderate medium modification effects in central $\sqrt{s_{NN}} = 200$ GeV collisions, even in the $d+Au$ system, that increase the production of protons and kaons relative to pions. The PHENIX measurement of particle species dependent R_{dAu} in [26] at lower p_T suggests that the increased particle production relative to pions is dominantly proton and not kaon production.

IV. SUMMARY

We have measured the centrality dependence of charged hadron production at midrapidity in $d+Au$ collisions, as well as in $p+Au$ and $n+Au$ collisions that are tagged by a spectator nucleon from the deuteron nucleus. The hadron yields in $p+Au$ and $n+Au$ collisions are iden-

tical within our experimental uncertainty. Using the $p+p$ data from same energy, we calculated the nuclear modification factors R_{dAu} and R_{NAu} for various centrality selections. Within this analysis and its experimental uncertainty, there is no difference between R_{dAu} and R_{NAu} . Instead of a strong suppression as predicted by some color glass condensate models [9], an excess of hadron production is seen at $p_T > 2$ GeV/ c , consistent with enhancement due to the Cronin effect. The magnitude of the Cronin effect is independent of the number of additional scatterings ($\nu - 1$) within the limits of our uncertainties. We also studied the ratio of charged hadron yield to pion yield. We found that the charged pions account for about 60% of the charged hadrons at $p_T > 3$ GeV/ c , with a slightly larger value in central $d+Au$ collisions. This implies that R_{dAu} for protons and kaons remains close to one at higher p_T .

Acknowledgments

We thank the staff of the Collider-Accelerator and Physics Departments at Brookhaven National Laboratory and the staff of the other PHENIX participating institutions for their vital contributions. We acknowledge support from the Office of Nuclear Physics in the Office of Science of the Department of Energy, the National Science Foundation, Abilene Christian University Research Council, Research Foundation of SUNY, and Dean of the College of Arts and Sciences, Vanderbilt University (U.S.A); Ministry of Education, Culture, Sports, Science, and Technology and the Japan Society for the Promotion of Science (Japan); Conselho Nacional de Desenvolvimento Científico e Tecnológico and Fundação de Amparo à Pesquisa do Estado de São Paulo (Brazil); Natural Science Foundation of China (People's Republic of China); Centre National de la Recherche Scientifique, Commissariat à l'Énergie Atomique, and Institut National de Physique Nucléaire et de Physique des Particules (France); Ministry of Industry, Science and Technologies, Bundesministerium für Bildung und Forschung, Deutscher Akademischer Austausch Dienst, and Alexander von Humboldt Stiftung (Germany); Hungarian National Science Fund, OTKA (Hungary); Department of Atomic Energy (India); Israel Science Foundation (Israel); Korea Research Foundation and Korea Science and Engineering Foundation (Korea); Ministry of Education and Science, Russia Academy of Sciences, Federal Agency of Atomic Energy (Russia), VR and the Wallenberg Foundation (Sweden); the U.S. Civilian Research and Development Foundation for the Independent States of the Former Soviet Union; the US-Hungarian NSF-OTKA-MTA; and the U.S.-Israel Binational Science Foundation.

-
- [1] K. Adcox *et al.* (PHENIX Collaboration), Phys. Rev. Lett. **88**, 022301 (2002).
- [2] S. S. Adler *et al.* (PHENIX Collaboration), Phys. Rev. Lett. **91**, 072301 (2003).
- [3] S. S. Adler *et al.* (PHENIX Collaboration), Phys. Rev. C **69**, 034910 (2004).
- [4] M. Gyulassy and M. Plumer, Phys. Lett. **B243**, 432 (1990); X. N. Wang and M. Gyulassy, Phys. Rev. Lett. **68**, 1480 (1992).
- [5] S. S. Adler *et al.* (PHENIX Collaboration), Phys. Rev. Lett. **97**, 052301 (2006).
- [6] S. S. Adler *et al.* (PHENIX Collaboration), Phys. Rev. C **71**, 051902 (2005).
- [7] S. S. Adler *et al.* (PHENIX Collaboration), Phys. Rev. Lett. **91**, 172301 (2003)
- [8] V. Greco, C. M. Ko and P. Lévai, Phys. Rev. Lett. **90**, 202302 (2003).
- [9] D. Kharzeev, Yu. V. Kovchegov and K. Tuchin, Phys. Rev. D **68**, 094013 (2003).
- [10] J. W. Cronin *et al.*, Phys. Rev. D **11**, 3105 (1975).
- [11] P. B. Straub *et al.*, Phys. Rev. Lett. **68**, 452 (1992).
- [12] S. S. Adler *et al.* (PHENIX Collaboration), Phys. Rev. Lett. **91**, 072303 (2003).
- [13] S. S. Adler *et al.* (PHENIX Collaboration), Phys. Rev. Lett. **98**, 172302 (2007).
- [14] M. Lev and B. Peterson, Z. Phys. C **21**, 155 (1983).
- [15] K. Adcox *et al.* (PHENIX Collaboration), Nucl. Instrum. Meth. **A499**, 469-602 (2003).
- [16] S. S. Adler *et al.* (PHENIX Collaboration), Nucl. Instrum. Meth. **A499**, 593 (2003).
- [17] C. Adler *et al.* (STAR Collaboration), Nucl. Instrum. Meth. **A499**, 433 (2003).
- [18] T. A. Armstrong *et al.*, Nucl. Instrum. Meth. **A406**, 227 (1998).
- [19] S. White, AIP Conf.Proc. **792**, 527 (2005).
- [20] S. S. Adler *et al.* (PHENIX Collaboration), Phys. Rev. Lett. **94**, 082302 (2005).
- [21] L. Hulthén and M. Sagawara, Handbuch der Physik, edited by S. Flügge (Springer-Verlag, New York, 1957), Vol. 39. **39**, (1957).
- [22] A. F. Krutov and V. E. Troitsky, Phys. Rev. C **76**, 017001 (2007).
- [23] R. J. Glauber and G. Matthiae, Nucl. Phys. **B21**, 135 (1970).
- [24] T. Sjöstrand, L. Lönnbald and S. Mrenna, arXiv:hep-ph/0108264 (2001).
- [25] V. Ryabov [for PHENIX Collaboration], Nucl. Phys. **A774**, 735 (2006).
- [26] S. S. Adler *et al.* (PHENIX Collaboration), Phys. Rev. C **74**, 024904 (2006).
- [27] J. Adams *et al.* [STAR Collaboration], Phys. Lett. **B637**, 161 (2006).
- [28] S. S. Adler *et al.* (PHENIX Collaboration), Phys. Rev. C **69**, 034909 (2004).
- [29] S. S. Adler *et al.* (PHENIX Collaboration), Phys. Rev. Lett. **95**, 202001 (2005)
- [30] Y. Zhang *et al.*, Phys. Rev. C **65**, 034903 (2002).
- [31] X. N. Wang, Phys. Rev. C **61**, 064910 (2000); Y. Zhang *et al.*, Phys. Rev. C **65**, 034903 (2002).
- [32] B. Z. Kopeliovich *et al.*, Phys. Rev. Lett. **88**, 232303 (2002). A. Accardi and D. Treleani, Phys. Rev. D **64**, 116004 (2001). I. Vitev and M. Gyulassy, Phys. Rev. Lett. **89**, 252301 (2002)
- [33] A. Accardi, arXiv: hep-ph/0212148.
- [34] B. Alper *et al.* (British-Scandinavian Collaboration), Nucl. Phys. **B100**, 237 (1975).